

Direct observation of light focusing by single photoreceptor cell nuclei

Zuzanna Błaszczak,¹ Moritz Kreysing,^{1,2} and Jochen Guck^{1,3,*}

¹*Cavendish Laboratory, Department of Physics, University of Cambridge, J.J. Thompson Avenue, Cambridge, CB3 0HE, UK*

²*Max Planck Institute of Molecular Cell Biology and Genetics, Pfotenhauerstrasse 108, Dresden 01307, Germany*

³*Biotechnology Center, Technische Universität Dresden, Tatzberg 47/49, Dresden 01307, Germany*

[*jochen.guck@tu-dresden.de](mailto:jochen.guck@tu-dresden.de)

Abstract: The vertebrate retina is inverted with respect to its optical function, which requires light to pass through the entire tissue prior to detection. The last significant barrier for photons to overcome is the outer nuclear layer formed by photoreceptor cell (PRC) nuclei. Here we experimentally characterise the optical properties of PRC nuclei using bright-field defocusing microscopy to capture near-field intensity distributions behind individual nuclei. We find that some nuclei efficiently focus incident light confirming earlier predictions based on comparative studies of chromatin organisation in nocturnal and diurnal mammals. The emergence of light focusing during the development of mouse nuclei highlights the acquired nature of the observed lens-like behaviour. Optical characterisation of these nuclei is an important first step towards an improved understanding of how light transmission through the retina is influenced by its constituents.

© 2014 Optical Society of America

OCIS codes: (330.0330) Vision, color, and visual optics, (330.4594) Optical effects on vision, (330.4875) Optics of physiological systems, (330.5370) Physiological optics, (330.7331) Visual optics, receptor optics

References and links

1. G. Horvath and D. Varju, *Polarized light in animal vision: Polarization patterns in nature* (Springer, 2004).
2. I. C. Cuthill, J. C. Partridge, A. T. Bennett, S. C. Church, N. S. Hart, and S. Hunt, "Ultraviolet vision in birds," (Academic Press, 2000), pp. 159 – 214.
3. M. F. Land, "The physics and biology of animal reflectors," *Prog. Biophys. Mol. Biol.* **24**, 75–106 (1972).
4. T. M. Jordan, J. C. Partridge, and N. W. Roberts, "Non-polarizing broadband multilayer reflectors in fish," *Nat. Photonics* **6**, 759–763 (2012).
5. M. Kreysing, R. Pusch, D. Haverkate, M. Landsberger, J. Engelmann, J. Ruiter, C. Mora-Ferrer, E. Ulbricht, J. Grosche, K. Franze, S. Streif, S. Schumacher, F. Makarov, J. Kacza, J. Guck, H. Wolburg, J. K. Bowmaker, G. von der Emde, S. Schuster, H.-J. Wagner, A. Reichenbach, and M. Francke, "Photonic crystal light collectors in fish retina improve vision in turbid water," *Science* **336**, 1700–1703 (2012).
6. G. T. D. Francia, "Retina cones as dielectric antennas," *J. Opt. Soc. Am.* **39**, 324–324 (1949).
7. R. L. Sidman, "The structure and concentration of solids in photoreceptor cells studied by refractometry and interference microscopy," *J. Biophys. Biochem. Cytol.* **3**, 15–30 (1957).
8. J. M. Enoch, "Optical properties of the retinal photoreceptors," *J. Opt. Soc. Am.* **53**, 71–85 (1963).
9. W. Stiles, "The luminous efficiency of monochromatic rays entering the eye pupil at different points and a new colour effect," *Proc. R. Soc. B* **123**, 90–118 (1937).
10. G. Westheimer, "Directional sensitivity of the retina: 75 years of stiles-crawford effect," *Proc. Biol. Sci.* **275**, 2777–2786 (2008).

11. M. P. Rowe, N. Engheta, S. S. Easter, Jr, and E. N. Pugh, Jr, "Graded-index model of a fish double cone exhibits differential polarization sensitivity," *J. Opt. Soc. Am. A. Opt. Image. Sci. Vis.* **11**, 55–70 (1994).
12. K. Arnold and C. Neumeyer, "Wavelength discrimination in the turtle *pseudemys scripta elegans*," *Vision Res.* **27**, 1501–1511 (1987).
13. J. Bowmaker, "Colour vision in birds and the role of oil droplets," *Trends in Neurosciences* **3**, 196 – 199 (1980).
14. H. B. Barlow, "What causes trichromacy? A theoretical analysis using comb-filtered spectra," *Vision Res.* **22**, 635–643 (1982).
15. V. Govardovskii, "On the role of oil drops in colour vision," *Vision Res.* **23**, 1739 – 1740 (1983).
16. M. Vorobyev, "Coloured oil droplets enhance colour discrimination," *Proc. Biol. Sci.* **270**, 1255–1261 (2003).
17. K. Franze, J. Grosche, S. N. Skatchkov, S. Schinkinger, C. Foja, D. Schild, O. Uckermann, K. Travis, A. Reichenbach, and J. Guck, "Müller cells are living optical fibers in the vertebrate retina," *Proc. Natl. Acad. Sci. USA* **104**, 8287–8292 (2007).
18. I. Solovei, M. Kreysing, C. Lanctôt, S. Kösem, L. Peichl, T. Cremer, J. Guck, and B. Joffe, "Nuclear architecture of rod photoreceptor cells adapts to vision in mammalian evolution," *Cell* **137**, 356–368 (2009).
19. D. Comings, "Arrangement of chromatin in the nucleus," *Hum. Genet.* **53**, 131–143 (1980).
20. S. de Nooijer, J. Wellink, B. Mulder, and T. Bisseling, "Non-specific interactions are sufficient to explain the position of heterochromatic chromocenters and nucleoli in interphase nuclei," *Nucleic. Acids. Res.* **37**, 3558–3568 (2009).
21. K. Finan, P. R. Cook, and D. Marenduzzo, "Non-specific (entropic) forces as major determinants of the structure of mammalian chromosomes," *Chromosome Res.* **19**, 53–61 (2011).
22. T. Sexton, H. Schober, P. Fraser, and S. M. Gasser, "Gene regulation through nuclear organization," *Nature Structural and Molecular Biology* **14**, 1049–1055 (2007).
23. M. Kreysing, L. Boyde, J. Guck, and K. J. Chalut, "Physical insight into light scattering by photoreceptor cell nuclei," *Opt. Lett.* **35**, 2639–2641 (2010).
24. P. Sarthy and D. M. Lam, "Isolated cells from the mammalian retina," *Brain Res.* **176**, 208–212 (1979).
25. K. J. Chalut, A. E. Ekpenyong, W. L. Clegg, I. C. Melhuish, and J. Guck, "Quantifying cellular differentiation by physical phenotype using digital holographic microscopy," *Integr. Biol. (Camb)* **4**, 280–284 (2012).
26. R. Barer and S. Joseph, "Refractometry of living cells part I. Basic principles," *Q. J. Microsc. Sci.* **95**, 399–423 (1954).
27. Y. Sun, S. Duthaler, and B. J. Nelson, "Autofocusing in computer microscopy: selecting the optimal focus algorithm," *Microsc. Res. Tech.* **65**, 139–149 (2004).
28. A. F. Oskooi, D. Roundy, M. Ibanescu, P. Bermel, J. Joannopoulos, and S. G. Johnson, "Meep: A flexible free-software package for electromagnetic simulations by the FDTD method," *Computer Physics Communications* **181**, 687–702 (2010).
29. J. Bowmaker and H. J. Dartnall, "Visual pigments of rods and cones in a human retina," *J. Physiol.* **298**, 501–511 (1980).
30. E. N. Pugh, Jr and T. D. Lamb, "Amplification and kinetics of the activation steps in phototransduction," *Biochim. Biophys. Acta* **1141**, 111–149 (1993).
31. Y. Geng, L. A. Schery, R. Sharma, A. Dubra, K. Ahmad, R. T. Libby, and D. R. Williams, "Optical properties of the mouse eye," *Biomed. Opt. Express.* **2**, 717–738 (2011).
32. Y. Geng, A. Dubra, L. Yin, W. H. Merigan, R. Sharma, R. T. Libby, and D. R. Williams, "Adaptive optics retinal imaging in the living mouse eye," *Biomed. Opt. Express.* **3**, 715–734 (2012).

1. Introduction

Animal eyes show many amazing adaptations to their environment, such as detecting polarisation of light [1], seeing in ultraviolet [2] or evolving photonic crystal light reflectors and collectors [3–5]. Yet the optical consequences of the inverted structure of the vertebrate retina where, strangely, the photosensitive layer sits at the back of the tissue with respect to the incident light are still poorly understood. Before the light can be absorbed by the photoreceptor cell (PRC) outer segments it needs to travel through hundreds of microns of living neuronal tissue. Despite being considered transparent, cells that make up the retina are heterogeneous phase objects with organelles giving rise to refractive index (RI) modulation on a lengthscale comparable to the wavelength of visible light. Whereas this general property of biological cells renders other tissues, such as the dermis, opaque, the retina requires incident light to reach the light sensors with minimum scattering or absorption.

Extraordinarily, nature has also evolved ways of dealing with the problematic inverted structure of the retina. In the middle of the 20th century scientists developing theories of radar anten-

nas, light trapping and optical fibre waveguiding applied the new concepts to the outer segments of the light sensitive cells called photoreceptors to show that these segments act as optical fibres [6–8]. The description of the outer segments as optical fibres then seemed to rationalise the curious directional sensitivity of the retina known as the Stiles–Crawford effect [9, 10]. Such an optimisation of the cell to create an optical element was not only surprising but also gave impetus to the bottom up, cell type by cell type, approach to understanding the optical properties of the retina. And thus it was soon discovered that even more peculiar optimisations happen on a species specific level. For example, the graded index in the fish double cone has been suggested to contribute to light guiding [11]. Another well studied example of optical elements in the retina are the oil droplets found in the cones of diurnal birds. Since the carotenoid-filled oil droplets are found in the inner segments of the cones they selectively absorb light before it reaches the outer segments of the photoreceptors. Their exact function is still debated and there are arguments speaking for both the improvement of spatial vision [12] and for their role in colour vision [13–16] but it is certain that their *raison d'être* lies in optical processing of light before detection.

One of the most recent findings [17] showed that the shape and RI distribution of retinal glia cells known as Müller cells are optimised for supporting the light transport through the retina. These radial glial cells, which span two thirds of the retina, have an elongated cell body with a higher RI than their surroundings, they contain very few organelles and densely pack their cytoskeleton, which is oriented along the light direction. This creates a long cylindrical body with minimal obstacles for the propagating light. This results in a cell that acts as an optical fibre allowing the guidance of light from the inner limiting membrane all the way to the outer nuclear layer (ONL). Because the ONL sits anterior to the photosensitive outer segments it constitutes the last barrier in the path of the light coming from the Müller cells.

Solovei et al. showed that the internal structure of the PRC nuclei, which make up the ONL, differs between diurnal and nocturnal mammals [18]. The observed difference was found in the chromatin distribution within the nucleus. Chromatin is the protein mediated condensate of DNA that fills the cell nucleus. In a non-dividing nucleus chromatin is found in two phases that differ in protein and DNA density. As a likely consequence of the difference in mass density, the two chromatin phases are thought to differ in their RI [18]. Thus the distribution of the chromatin inside the cell nucleus was predicted to have a direct effect on light propagation.

The chromatin phase where the DNA is loosely packed in order to be accessible to transcriptional machinery is known as euchromatin and in the vast majority of cells it occupies the centre of the nucleus [19]. Where the DNA codes for inactive genes it is highly condensed in a chromatin phase referred to as heterochromatin. Heterochromatin, being more dense with DNA and proteins than euchromatin has a higher RI; it is distributed around the outer parts of the nucleus [19]. We will refer to this nuclear architecture as the conventional nuclear pattern and to the nucleus exhibiting such a pattern as a conventional nucleus. This conventional nuclear pattern has been shown to be driven by entropic forces [20, 21] and is thought to relate to transcriptional regulation [22]. It is ubiquitous and very well conserved.

As Solovei et al. have shown, PRC nuclei of nocturnal mammals do not share this architecture. In these nuclei the putatively high RI heterochromatin is found in the middle of the nucleus while the likely lower RI euchromatin forms a shell around the heterochromatin centre. Computer simulations based on interferometric phase shift measurements of the nuclei, which have suggested the difference in RI between heterochromatin and euchromatin, predicted that the inversion of the chromatin pattern in nocturnal PRC nuclei results in a lens-like behaviour of the nucleus [18, 23]. This, in turn, presumably improves light transport through the ONL, which could be the evolutionary advantage that justifies the deviation from a highly conserved cellular feature.

In this study we test the predictions of nuclear focusing experimentally. We measure and analyze the distribution of light behind individual PRC nuclei illuminated with a near unidirectional illumination and compare light fields of nuclei of both architectures. We also compare our results to the theoretical predictions presented in [18] and [23]. Our results provide direct evidence that the nuclei act as lenses and that there is a clear difference in the refractive power of nuclei from diurnal and nocturnal mammals, in line with the chromatin inversion reported in [18]. This information brings us one step closer to understanding how light interacts with the vertebrate retina; this knowledge is useful not purely in the understanding of the normal functioning of the tissue but can also help to advance current retina imaging modalities, such as optical coherence tomography.

2. Method

2.1. Sample preparation

2.1.1. Photoreceptor nuclei

We investigated the optical properties of porcine, adult and young mouse as well as rabbit photoreceptor cell (PRC) nuclei. Mice were sacrificed by cervical dislocation, rabbits were sacrificed by venous injection, both according to the Animals (Scientific Procedures) Act of 1986. Pig eyeballs were obtained from a local abattoir. Single PRC nuclei were obtained from retinas excised from the eyeballs as described in [24]. Mice and rabbit eyes were enucleated immediately after sacrificing the animal; they were opened with a blade and put into oxygenated extracellular (ECS) solution (110 mM NaCl, 3 mM KCl, 2 mM CaCl₂, 1 mM MgCl₂, 1 mM Na₂HPO₄, 0.25 mM glutamine, 10 mM HEPES, 11 mM glucose, 25 mM NaHCO₃) and on ice for transport to the preparation room. Pig eyes were opened up to 15 min after the animal was killed and the retinas were excised up to one hour afterwards. The excised retinas, cut into $2\text{mm} \times 2\text{mm}$ pieces were washed in PBS four times and incubated in 1ml PBS with papain enzyme (Roche Diagnostics) at 37°C to dissolve the extracellular matrix. To prevent clumping of cells caused by extracellular DNA, 0.5 μl of Deoxyribonuclease I (D5307-1000UN, 1 unit/ μl , DNase I, Sigma-Aldrich) was added to 1 ml of incubation solution. For successful dissociation of the retinas, papain concentrations and incubation times varied for each species and were as follows: a) young mice: 200 $\mu\text{g}/\text{ml}$ for 15 minutes; b) adult mice: 200 $\mu\text{g}/\text{ml}$ for 30 minutes; c) pigs: 100 $\mu\text{g}/\text{ml}$ for 30 minutes and d) rabbit: 30 $\mu\text{g}/\text{ml}$ for 30 minutes. The different protocols were used to obtain similar levels of retinal degradation after treatment. The samples were then washed with ECS to remove traces of the papain and the tissue was mechanically dissociated by gentle pipetting. The resulting suspension contained more than 60% PRC nuclei with the debris being formed of other nuclei, cell parts, axons or PRC outer segments. Representative images of the resulting suspension seen in Fig. 1 show that PRC nuclei are easily discerned from debris by their size and morphology. Staining of the nuclear suspension with a nucleic acid stain (Syto 63 Red Fluorescent Nucleic Acid Stain, Molecular Probes) showed some nuclei to be still surrounded by a layer of cytoplasm. However, due to their unusual shape, these were easily discriminated from the majority of extracted nuclei, which showed no signs of residual cytoplasm. Nuclei where the cytoplasm was not removed entirely were then not considered further.

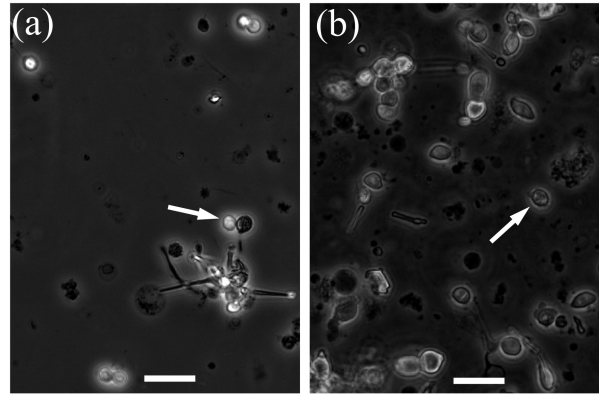


Fig. 1. Phase contrast images of the dissociated retina samples. Mouse PRC nuclei are easily discernible in (a) as round, bright, homogenous circles in phase contrast. Pig PRC nuclei in (b) show an elliptical shape and a heterogeneous distribution of light and dark parts. Scale bar in both images is $20\mu m$.

2.1.2. Silica microspheres

Silica microspheres (MSS005, diameter $5\mu m$ with standard deviation 15%, Whitehouse Scientific UK) were used as PRC nuclei mimics in control experiments to validate the experimental method. The RI of the microspheres was measured with digital holographic microscopy [25] as $n = 1.423 \pm 0.001$ and verified with immersion refractometry [26] and a novel technique presented in detail in Appendix B.

2.2. Direct imaging of light focusing

Light fields behind dielectric objects (PRC nuclei and silica microspheres) were captured using a standard bright field microscope setup with a piezoelectrically-driven objective to scan along the optical axis and capture images in $1.0\mu m$ steps. A small condenser aperture together with Köhler illumination were used to approximate unidirectional (plane wave) illumination and to allow comparison to simulations in [18, 23]. The smallest condenser setting of the microscope (Leica Confocal TC3 SP5) resulted in a numerical aperture $NA=0.03$. In order to avoid image aberrations due to non-optimal conditions (imaging partly inside the glass slide) an objective with an intermediate NA was chosen (HCX PL FLUOTRL 40×0.60 DRY). A bandpass filter with a pass region of $10nm$ and a central wavelength $\lambda = 500nm$ (Thorlabs, FB500-10) was placed in the illumination beam to ensure monochromaticity of the incident light.

2.3. Data analysis

Data stacks were processed in Matlab. Qualitative comparison of light fields was done by visually examining xz cross-sectional reconstructions of the intensity maps (Fig. 2(a) and 2(b)) and three-dimensional renderings of the light field (Fig. 2(c)). The cross-sections were taken through the middle of the dielectric object and were used to compare the amount of scatter introduced by the object, the modulation of light intensity and the shape of the focus. Quantitative data was obtained by measuring the focal length of the dielectric objects. The effective focal length of an object was defined as the distance between the centre of the object and the focus point. The focus point was determined by finding the plane maximising a function f defined as follows:

$$f = \frac{I_{max}}{\bar{I}}. \quad (1)$$

Here I_{max} and \bar{I} are the maximum and average intensities in a given plane respectively.

To find the centre of the nucleus we followed results from [27] and determined the maximum of the normalised variance function (Eq. 2) given below.

$$F = \frac{1}{HW\mu} \sum_W \sum_H (I(x,y) - \mu)^2 \quad (2)$$

Here H is the height of the image, W is the width, μ is the average intensity of the image and $I(x,y)$ is the greyscale intensity value of the pixel with coordinates (x,y) . In around 20% of cases, the algorithm pinpointed a plane that very clearly could not be the in-focus plane. In such situations the algorithm was rerun on a predefined interval of images of a manually identified focus.

The cross sectional images were plotted with a false colour map showing the amplitude of the light intensity in units of average incident intensity. In three dimensional renderings the light intensity was shown as surfaces of constant intensity (iso-surfaces) also defined in units of the incident intensity.

2.4. Simulations

Finite difference time domain (FDTD) simulations and Mie theory calculations were implemented to model light transmission through dielectric objects. Comparison between experiments and computer simulations provided a way to verify the experimental method and to test predictions based on previous simulations in [18].

FDTD simulations are grid-based simulations where an electromagnetic system is modeled by evolving Maxwell's equations over time using discrete time steps. Following the methods described in [18], the simulations were implemented with MEEP, an open source software package [28]. Simulations were run in two and three dimensions at a vacuum wavelength of 500nm, which corresponds roughly to the wavelength of highest rod sensitivity [29]. To avoid diffraction and reflections from the boundaries of the computational region periodic boundary conditions in transverse dimensions were combined with absorbing boundaries (perfectly matching layers) at the end of the computational cell. The nuclei were modeled as spherical core-shell type particles where the shell and core were assigned refractive index values of either heterochromatin or euchromatin, initially according to values quoted in [18, 23], that is $n_h = 1.415$ for heterochromatin and $n_e = 1.385$ for euchromatin. The simulations were run until the induced fields reached a steady state (roughly within 200 optical periods), at which point the intensity distribution was output as an image. For quantitative comparisons the effective focal length of the dielectric objects in FDTD simulations was defined as the distance between the centre of the object and the focus point determined using the algorithm described above (Eq. 1).

Mie theory calculations were done numerically in a Matlab program as described previously in [23]. The program solves Mie equations for the intensity of an electromagnetic plane wave after it propagates through a dielectric sphere. The effective focal length was defined as the radius of the sphere plus the z coordinate of the peak in the plot of intensity as a function of distance behind the sphere.

3. Results

3.1. Light transmission properties of photoreceptor nuclei

In this study we have developed a method of visualising near field light distributions behind PRC nuclei by taking successive images of a Köhler illuminated nucleus and 40 microns of space below it at 1 micron intervals. The result are three dimensional intensity maps of the light

field in and around the diffracting object. To analyse the data, intensity maps were reconstructed in the xz plane to create cross-sectional views through the centre of the nucleus and the light pattern around it. The xz reconstructions allowed a direct comparison between optical properties of conventional and inverted nuclei.

We first investigated adult mouse nuclei. Mice are nocturnal animals and their PRC nuclei have an inverted nuclear pattern with a putative low RI euchromatin shell around a higher RI heterochromatin core [18]. The reconstructed cross sectional view through the light field of an adult mouse nucleus, Fig. 2(a), shows a clear focusing of the incident light by a typical nucleus. This confirms earlier predictions [18] that an inverted nucleus focuses incident light in a lens-like fashion. The light at the focus is amplified to about 8 times the incident intensity with an effective focal length of $14 \pm 1 \mu\text{m}$. Here the effective focal length is defined as the distance between the centre of the nucleus and the focus point and is calculated using the algorithm described in section 2.3. The light field is rotationally symmetric around the z axis and the high intensity region extends over about 20 microns. The isotropy and correct scaling of the imaged light fields was confirmed by comparison of the effective focal length of nuclear mimics (silica microspheres) measured experimentally to focal lengths predicted by Mie theory and computer simulations. Experimentally measured focal length of the microspheres was $13 \pm 1 \mu\text{m}$ (standard error of mean). This agreed with the focal length of $13.3 \pm 0.8 \mu\text{m}$ predicted from Mie theory calculations and $14 \pm 1 \mu\text{m}$ given by FDTD simulations. We thus conclude that the axial scale of the light fields collected with the technique presented here is correct and the images do not require rescaling.

We next studied the intensity maps of porcine nuclei (Fig. 2(b)). Pigs are diurnal animals and their PRC nuclei exhibit the conventional nuclear pattern found in almost all cell nuclei. Although a focus-like region is also visible in the light distribution for the pig nucleus, it is fundamentally different from the one observed for adult mice nuclei. The light distribution for the pig nucleus shows considerably more scattering around the edges and a broken rotational symmetry around the z axis. This particular nucleus, which is typical for all the 31 nuclei investigated, has an effective focal length of $26 \pm 1 \mu\text{m}$ and the light amplification level in the high intensity region stays below 6. Such a light field distribution is reminiscent of the light distribution behind an object with a simple step function phase shift and can be explained by diffraction from the edges as illustrated in Fig. 3.

The difference in the transmission properties between the conventional nuclei of pigs and the inverted nuclei of adult mice is statistically significant at the $p = 0.05$ level using an unpaired t test with Welch's correction. As can be seen in Fig. 2(d) photoreceptor nuclei of pigs have a mean effective focal length that is twice the focal length of adult mice ($12 \pm 1 \mu\text{m}$). Moreover, light field patterns of adult mice nuclei show little variation from nucleus to nucleus, hence the small error bars in Fig. 2(d) and the tight distribution of the focal length measurements. On the other hand, the large error bars and widely scattered focal length measurements for porcine nuclei reflect the large variations between those light fields. Additional measurements were also performed with rabbit and young mice nuclei. Rabbits are crepuscular animals and their PRC nuclei have an inverted nuclear pattern resembling the one found in adult mice nuclei. However, unlike the adult mice nuclei which are spherical, the rabbit nuclei maintain the prolate spheroid shape common to conventional nuclei such as those of pigs. Despite the difference in shape and size, both rabbit and adult mouse nuclei have comparable effective focal lengths ($9 \pm 1 \mu\text{m}$ and $12 \pm 1 \mu\text{m}$ respectively) and exhibit a lens-like behaviour. On the other hand, young mouse nuclei show half the refractive power of adult mouse nuclei. This can be explained by the fact that mice are born with PRC nuclei exhibiting a conventional pattern. This pattern is slowly inverted during the first 28 days after birth, at which point all the PRC nuclei in the mouse retina display an inverted pattern. As seen in Fig. 2(d), the non-inverted nuclei of young mice

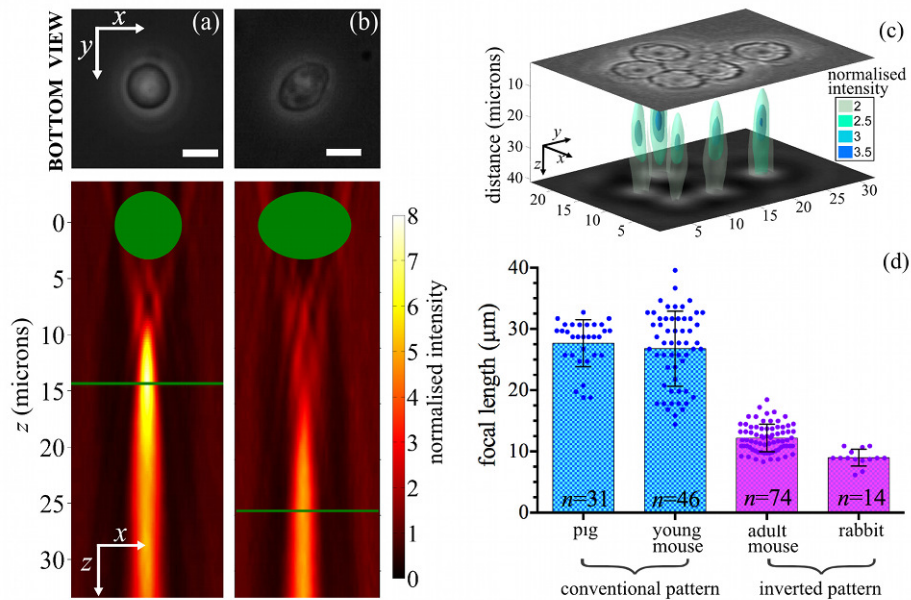


Fig. 2. Light focusing by individual PRC nuclei. (a-b) Phase contrast images of representative nuclei and the xz reconstructions of the intensity maps for adult mouse (a) and porcine (b) nuclei. In xz reconstructions light is incident from the top and travels in downward z direction. Green circle and ellipse indicate the position and size of the mouse and pig nuclei respectively. Green line indicates the focus point for measuring the effective focal length. Scale bars in phase contrast images are $5 \mu\text{m}$. c) Three dimensional reconstruction of the foci generated by adult mouse nuclei. Light is incident at the top and travels in downward z direction. The top plane shows a nucleus cluster in focus; below it is the light field reconstructed by generating isosurfaces at four intensities. d) Effective focal lengths of photoreceptor cell nuclei of three different species. The number of nuclei measured varied between species and is indicated for each animal by n . Dots in the bar graph are individual measurements. The difference between conventional and inverted patterns is statistically significant at the $p = 0.05$ level.

have the same optical properties as the porcine nuclei and show a similar variation in light field distributions. This set of experiments clearly demonstrates that the nocturnal lifestyle and the accompanying chromatin inversion is directly linked to the optical properties of these nuclei.

3.2. Computer models of adult mice and porcine nuclei

For the direct comparison of simulation results to experiments a representative xz reconstruction was chosen to illustrate the light field distributions observed for PRC nuclei of adult mice and pigs.

Adult mouse nuclei

In FDTD simulations adult mouse nuclei were modelled as a sphere with a high RI core (n_c) and lower RI shell (n_s) in a suspension medium with $n = 1.335$. The closest similarity between experimental and simulation light fields was achieved for a three-dimensional simulation with $r_c : r_s = 0.8$ and refractive index ratio $m = n_s : n_c = 1.02$ between heterochromatin and euchromatin regions respectively (Fig. 4(b)). Because the computational memory required to

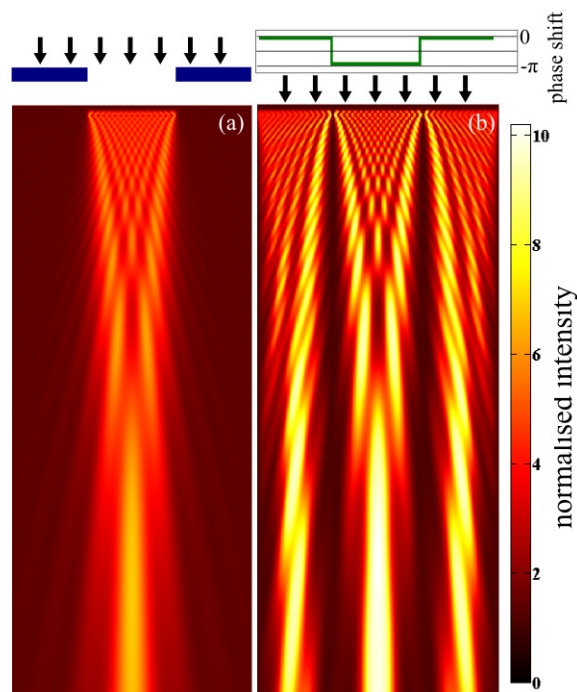


Fig. 3. Simulated light distribution for a slit and step function phase profile. In (a) light incident from the top passes through a slit whose dimensions are indicated by the space between the blue rectangles. In (b) the slit is replaced by step function phase profile where light is retarded by $-\pi$. The higher intensity region in the both diffraction patterns are the same and are a result of light diffraction from the edges.

run three-dimensional simulations poses constraints on the size of the computational box (required memory scales like $dimension^3$), we focus on two dimensional simulations to provide qualitative understanding. Although the focus in the two-dimensional simulation (Fig. 4(c)) is narrower than the one observed experimentally (Fig. 4(a)) and the focal lengths differs by $2\mu m$, the two-dimensional simulation is able to reproduce the main features seen in the experimental reconstruction and would be an acceptable choice for simulations involving multiple inverted nuclei. The robustness of the inverted nucleus model was investigated by varying the RI and radii of the core and shell; the results of this are presented in Appendix A.

Porcine nuclei

Following the work in [18, 23] conventional nuclei were first modeled in 2D as an inverse version of the adult mouse model, that is, a simple circular object with now the high RI in the shell and the low RI euchromatin in the core. The resulting simulation shows the long focal length and increased lateral light scatter observed in experiments (Fig. 5(a) and Fig. 5(b)) but does not capture the details of light scattering from the edges of the nucleus. Modifications of parameters such as the RI of core and shell and their relative radii were not enough to recapture those details. Hence we introduced a more sophisticated model, which took into account morphological differences between conventional and inverted nuclei observed in phase contrast images (Fig. 5(a)). The circular shape of the conventional models was first replaced by an ellipse (data not shown) and then by an ellipse with an irregular interface between the chromatin regions

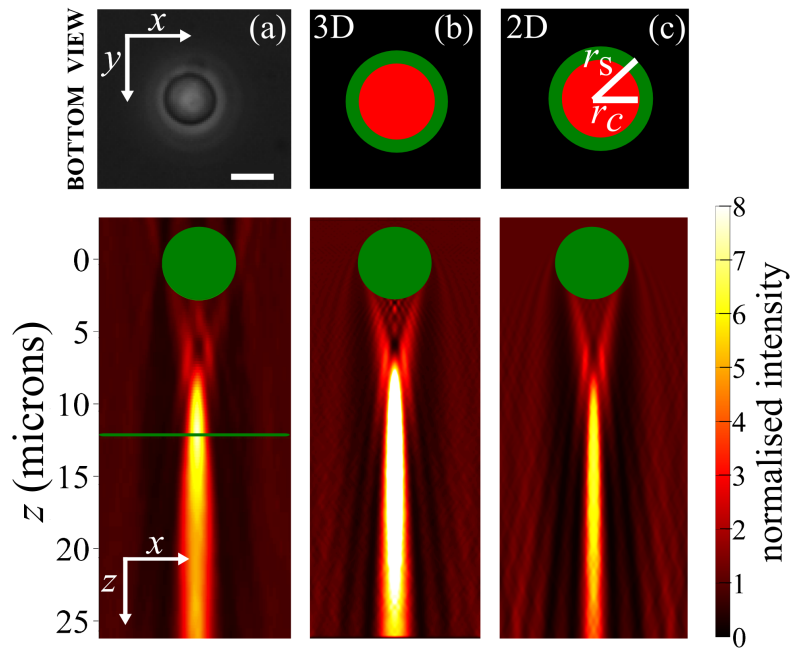


Fig. 4. Modelling an adult mouse nucleus in FDTD simulations. (a) Representative phase contrast image and xz reconstruction of experimentally measured intensity map of an adult mouse nucleus. (b-c) FDTD simulations most closely matching experimental light fields. (b) Three-dimensional simulation of an inverted nucleus using a spherical core-shell model shows good agreement with experiment. Here $r_c = 4\mu m$ and $r_s = 5\mu m$. (c) The same model implemented in two-dimensions shows a longer focal length but captures main optical behaviour of an adult mouse nucleus. Green circles in xz reconstructions indicate the position and size of the nuclei or nuclear models, green line indicates the focus plane. Scale bar in phase contrast image is $5\mu m$.

(Fig. 5(c)). Elliptical models with both the smooth and irregular border led to light distributions displaying a larger focal lengths, wide and pronounced side-lobes (where the intensity drops to zero) as well as very low levels of light amplification and were arguably a worse fit to the experimental data than the light fields of the simple circular model.

However, we have seen with the inverted model of the mouse nucleus, that three-dimensional simulations show a better fit to experimentally observed data than two-dimensional simulations. Thus we decided to investigate whether it would be more appropriate to model the elliptical shape in three dimensions. In three dimensions the ellipse was scaled to a prolate spheroid and was initially modelled with the major axis normal to the incident light direction (Fig. 5(d)), as this is the orientation manifested by single nuclei during experiments. The resulting light field is an improvement over the two dimensional elliptical model; the light field has a shorter focal length, higher light amplification and narrower, less pronounced side-lobes more in line with the light fields observed experimentally. Following this promising result, the three-dimensional simulation was repeated with the nucleus rotated 90° (Fig. 5(e)) to reflect the orientation of the conventional nuclei in the outer nuclear layer in the retina. The result clearly shows that for an ellipsoidal nucleus the focal length is heavily dependent on the orientation of the nucleus with respect to the incident light. However, even the shorter focal length of conventional nuclei oriented with its major axis parallel to incident light is longer than the focal length of inverted

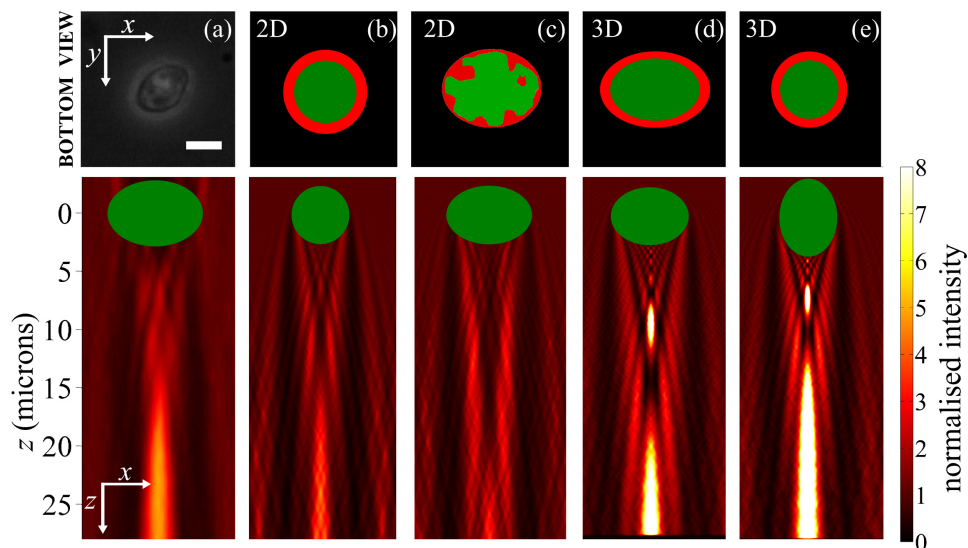


Fig. 5. Modelling the porcine nucleus in FDTD simulations. (a) Representative phase contrast image and xz reconstruction of experimentally measured intensity map of a porcine nucleus. (b-e) Three different models of the pig nucleus were investigated in FDTD simulations: simple spherical core-shell model in two dimensions (b); ellipse model with irregular interface between euchromatin and heterochromatin in two dimensions (c); prolate spheroid model in three dimensions with major axis normal (d) and parallel (e) to incident light direction. Green ellipses in xz reconstructions indicate the position and size of the nuclei or nuclear models while blue line indicates interface between water and glass in the simulation. Scale bar in phase contrast image is $5\mu m$.

nuclei.

4. Discussion

Our results clearly show that PRC nuclei of nocturnal mammals (mouse, rabbit) focus incident light in a lens-like behaviour, thus confirming earlier predictions based on the measurement of nuclear phase profiles and simulations of their effect on light propagating through the nuclei [18, 23]. This experimentally verified lensing effect is not trivial. It arises as a result of the redistribution of the chromatin phases inside the nucleus to form an inverted nuclear pattern. This rearrangement in mice happens throughout the first month after birth and, as we have shown, corresponds to a drastic shortening of the effective focal length of the nucleus (from about $27\mu m$ in young mice to about $12\mu m$ in adult mice, see Fig. 2(d)). Nocturnal mammals are born with conventional PRC nuclei, which in the first instance need to fulfill their normal transcriptional function. During development the nuclei acquire a specialized physical function in addition to their normal biological function, which transforms the nuclei into lenses. For porcine and young mouse nuclei we observe a significantly different behaviour. The conventional chromatin pattern in these nuclei leads to a diffraction-like intensity distribution behind the nuclei. The observed long focal length (above $20\mu m$) is partly explained by the formation of a Poissonian spot and secondary intensity maxima such as those visible for a simple step phase shift. It should be emphasized that the measured focal lengths are likely to be different (longer) in the retina as the refractive index mismatch between the nuclei and the surrounding extracellular matrix is lower than the mismatch between the nuclei and water encountered in

the measurements. Likewise the normalized intensity increase would be lower at the focus than predicted and measured. However, the important aspect is that the optical models of the nuclei identified here by comparing experiments in water with simulations in water can then be used to simulate the focusing of the nuclei once placed in a different environment with a refractive index more appropriate for the retina.

Throughout the experiments plane wave illumination was attempted rather than the more physiologically correct convergent light encountered by mouse nuclei in the ONL. This was an informed choice based on the fact that plane waves allow the proper experimental determination of the focal length of individual nuclei. Once the focal length, and the light field behind the nuclei have been determined, they can be compared to corresponding simulations, where of course the same illumination conditions have to be used. This in turn allows us to come up with realistic optical models of the nuclei. With these improved nuclear models we can then take into account the actual convergence present in the mouse eye. And thus, the inverted nucleus can be successfully modeled in FDTD simulations as a sphere with a low RI shell surrounding a core with an RI only 2% higher with absolute refractive index values of $n_e = 1.37$ and $n_h = 1.40$. However, the $r_c : r_s$ ratio of the model does not fully correspond to the biochemically defined hetero- and euchromatin regions seen in fluorescent images [18]. This suggests that there is no optically well defined core and shell region, but a gradual change. Nevertheless the model still allows to capture the essential optical properties in a useful way.

For the conventional nucleus the simulation models required to capture all experimentally observed features were more involved. In two dimensional simulations, the nuclear model, which seemingly resembles the morphology of a porcine nucleus (elliptical, with a rough heterochromatin-euchromatin interface) does not capture the optical properties observed in experiments as well as a simple circular model does. Due to gravity, the conventional nuclei in the experiments all lay flat on the glass slide. We modeled the spheroid with its major axis perpendicular to incident light in the first instance. However, in the retina, the orientation of the conventional nuclei is more varied. Various tilt angles in the range of 0 to 20° have been observed in unpublished TEM images of diurnal retinas obtained by our collaborators. Computer simulations with a spheroid whose major axis is parallel to the incident light show a strikingly different light field distribution to that of a spheroid rotated 90° (cf Fig. 5 (d) and (e)). This suggests that the light transmission through conventional nuclei depends to a large extent on the angle between the major axis of the nucleus and the direction of the incident light. The models of conventional nuclei required lower absolute RI values of heterochromatin and euchromatin ($n_e = 1.36$ and $n_h = 1.39$) than models of inverted nuclei. This can be understood in light of the larger conventional nuclei's larger volume and thus a putatively lower density of chromatin. However the ratio of heterochromatin and euchromatin RIs remains at 1.02 as expected.

One issue necessitating discussion is the authenticity of measurements performed on extracted nuclei, which could in principle have different physical properties than *in situ*. Firstly, we would argue that the distribution of heterochromatin and euchromatin, and its inversion in the case of nocturnal PRC nuclei, is stable and robust upon extraction from retina post mortem. After all, all normal cell nuclei *in vitro*, even after extensive culture, maintain their normal chromatin distribution with the heterochromatin predominantly found at the nuclear periphery. Secondly, we argue that the optical properties of heterochromatin and euchromatin are unchanged after death and extraction. After all, the main determinant of refractive index is the electron density of a material and in the case of the nucleus, the RI is dominated by the chromatin. Given that the distribution of hetero- and euchromatin (and of their mass) stays the same upon extraction with no noticeable change in nuclear volume measured, the RI of both chromatin phases should reflect the state *in vivo*. Even if the absolute RI did change, as a result of small volume changes induced by osmolarity, pH and/or ionic strength differences between the

imaging medium and the *in vivo* situation, previous work ([18,23]) has shown that the difference in focusing between the normal and the inverted nuclei is robustly found to be dependent on relative RI distributions and not on absolute values. Even a nuclear volume change *ex vivo* can not artificially induce the results we report. Thus, we are confident that the focal length measurement results we report here are truthful and meaningful representations of the focusing of these nuclei *in vivo*.

The spherical shape of the inverted nuclei in mice and rabbit PRCs and the smoothing of the heterochromatin and euchromatin layers inside the nuclei are complimentary changes that occur during inversion of the chromatin. As a result, the inverted nucleus exhibits point symmetry and its optical properties are effectively decoupled from its orientation. Thus the inverted nucleus not only focuses incident light more efficiently than a conventional nucleus, it also retains that focusing capability whatever its orientation. This is an important finding when the outer nuclear layer is taken into account as a whole. The outer nuclear layer in nocturnal retinæ is usually much thicker than in diurnal animals. For scotopic vision (vision at low light levels) the sensitivity of the rods is maximised for large photoreceptor outer segment volumes and small cross sections [30]. The latter aspect means that many rods are required to cover the entire retinal surface compared to cones in photopic vision at high light levels. But the PRC nuclei are always much thicker than the very thin rod segments, thus many rod nuclei have to pile up in many layers in the ONL. The geometrical constraints of the mouse retina imply that on average all segments of the 8-12 nuclei piled up in one column are assembled somewhere within the cross-sectional area of that column. It is conceivable that the relative thickness of the ONL is the principal reason for the energetically costly inversion of the chromatin architecture in nocturnal PRC nuclei. Any tactic that reduces lateral scatter (such as the inversion of the chromatin layers) in a thick outer nuclear layer is evolutionarily advantageous. The physiological, functional importance is obviously that the lack of lateral spread also reduces the chances of photons eventually being scattered backwards and not being detected. After all, photon catch is the paramount goal of scotopic vision, which then relates to the inversion only having been found in nocturnal mammals. There could also be aspects of improved motion detection at very low light levels due to the improved signal-to-noise ratio of information transmission in the inverted case. The spherical shape of the inverted nuclei additionally enables the retina to take advantage of the focusing properties of the rod nuclei without extra effort in arranging the nuclei within the layer. The regular spherical shape also allows a more efficient and regular packing, which reduces both the thickness of the ONL and the scatter. Of course, at present these are speculations and need to be substantiated in further research.

Recent imaging of photoreceptors in the living mouse eye using adaptive optics [31, 32] would seem to invalidate our ideas that PRC nuclei are scattering objects, since the photoreceptors are clearly seen at the proper packing density. However, a closer investigation of the observations at hand reveals this not to be the case. To obtain the images of photoreceptors in the living mouse eye as shown in [32], 120 images were recorded and averaged. This need for extensive averaging points to the fact that very few photons are actually reaching the detector. The high NA required and the confocal pinholes reject all scattered photons, which do not contribute to the image. The photons actually contributing to the image belong to a minor fraction of non-scattered (ballistic) photons. These ballistic photons are similar to those that reach our eye from a distant light source in a foggy night (and which allow one to relatively clearly see an object, e.g., moon or sun, if only enough photons are getting straight through). This explains why the researchers are able to image the photoreceptors in spite of most photons being scattered away. So, there is no inconsistency with our report. Moreover, the images of photoreceptors in the living mouse eye look different than the images of photoreceptors predicted theoretically (compare images in [31] and [32]). It is interesting to consider whether the

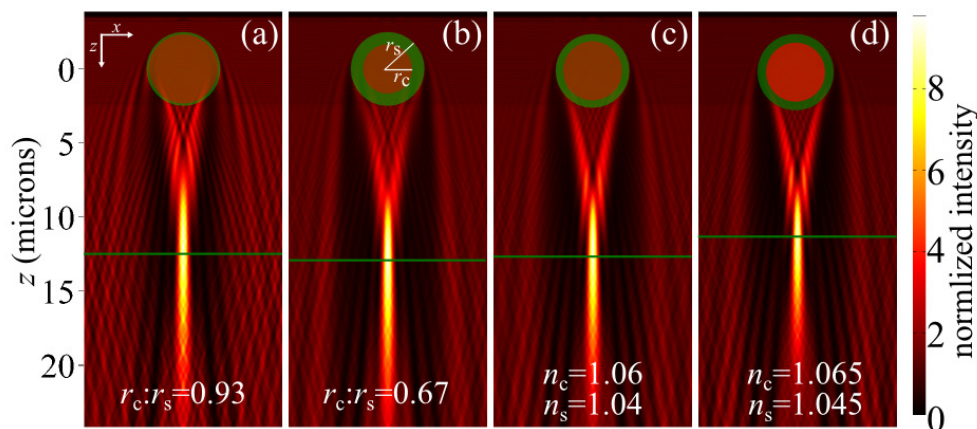


Fig. 6. Robustness of the inverted nucleus model. (a,b) The effect of varying the core (r_c) and the shell (r_s) radii of the nuclear mimic in FDTD simulations. The refractive index values of the core (n_c) and shell (n_s) are kept constant as are the total dimensions of the model (indicated by the circumference of the green circle). (a) $r_c = 4.6\mu\text{m}$ and $r_s = 5.0\mu\text{m}$ (b) $r_c = 3.4\mu\text{m}$ and $r_s = 5.0\mu\text{m}$. Changing the radii influences the light distribution in the vicinity of the nucleus but has no effect on the focal length (indicated by the green lines). (c,d) The effect of varying n_c and n_s on the light distribution while keeping $n_c : n_s = 1.019$ constant. Increasing the refractive index values of the core and shell (indicated by the saturation of the red and green circles) leads to a shorter focal length, a narrower focus and a shortened extent of the focus. In all simulations light is incident from the top and refractive indices are given as relative values.

discrepancy could be improved by considering refractive index heterogeneities in the retina in the theoretical modeling of that group.

The direct demonstration of contrasting light focusing by photoreceptor nuclei depending on the activity of the animals puts emphasis on the optical function of various cells in the retina. The retina's inverted structure means that the optical properties of the cells are just as important as their physiological function. It still remains to be understood how the collective arrangement of all these different cellular components then determines or improves the light transport of the retina as an entire tissue.

Appendix A

Fig. 6(a,b), shows that changing the ratio of core and shell radii ($r_c : r_s$) has only a slight effect on the effective focal length and the vertical extent of the focus. However, this ratio affects very strongly the light field at distances shorter than the focal length. The effective focal length as well as the axial extent of the focus are dependent on the refractive index values of the two chromatin layers. Figure 6(c,d) shows that increasing the refractive index value of both euchromatin and heterochromatin layers while keeping the $r_c : r_s$ and $n_c : n_s$ constant, resulted in a shorter focus and a smaller focal length. A smaller absolute value of refractive index gave a significantly extended focal spot with an appropriately longer focal length. One could also observe a small narrowing of the focus as the refractive index values were increased. A similar behaviour of the light field was seen when modifying the $n_c : n_s$ ratio of the inverted model while keeping the shell and core size constant (see Fig. 7).

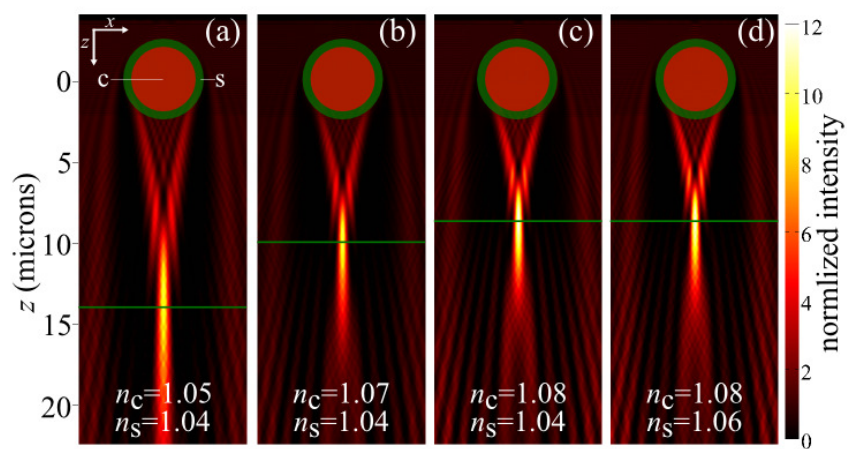


Fig. 7. Parameter space exploration of inverted nuclei models used in FDTD simulations. The refractive index values of the core (n_c) and shell (n_s), which represent regions of euchromatin and heterochromatin respectively are increased from (a-d). As refractive indices increase the extent of the focus gets smaller and narrower while the effective focal length shortens. $r_s = 5.0\mu m$ and $r_c = 4.0\mu m$ for all shown models. Here all refractive indices are given as relative values.

Appendix B

Refractive index determination

The refractive index of the silica microspheres used in the calibration test was determined by: 1) immersion refractometry; 2) digital holographic microscopy (DHM); and 3) a novel approach using wide field microscopy.

Briefly, immersion refractometry, first introduced for biological specimens by Barer [26] is a technique where the object of unknown refractive index is immersed in media with a known refractive index (we have used Cargille Labs refractive index matching liquids, combined set $n_D = 1.400 - 1.700$, cat. no. 18005) and inspected with a phase microscope. The behaviour of the halo around the sample changes as the ratio between the refractive index of the sample and the medium changes. A plot of the number of beads exhibiting one behaviour against the refractive index of the suspension medium can be plotted and the point of inflection gives the refractive index of the sample (Fig. 8). The precision of the method depends on the ability to create suspension media with a sufficiently small increment in refractive index.

Another method of measuring refractive indices is to use the DHM. The DHM is an interference microscope where an off-axis hologram is captured on a CCD camera. The hologram retains information about the phase of the illuminating wave as it propagates through the sample. The wave undergoes a phase change that depends explicitly on the difference in refractive index between the sphere and the surrounding medium. The phase change is captured in the image and the refractive index can be determined provided the size of the sample is known. For more details on the technique see [25].

The third method of measuring the refractive index was based on the wide field microscope setup described in section 2.2. Image stacks were collected for microspheres immersed in different refractive index oils (as in immersion refractometry) and xz views were created. The cross sections of beads suspended in a medium with a refractive index lower than the bead show a normal focus but immersion in a higher refractive index oil results in a formation of a virtual focus. Examples of this behaviour are shown in Fig. 9. Figure 9(a) shows the light distribution for a silica microsphere suspended in water and illuminated from above; the focus point is clearly below the bead whose position is indicated by the green circle. Figure 9(b) shows a similar bead, but suspended in an oil with a refractive index of 1.51. Here the focus point is above the microsphere. The refractive index of the immersion medium is increased until the focus becomes a virtual focus.

All three measurements of the refractive index of silica beads used as mimics of the photoreceptor nuclei agree. Immersion refractometry measurements gave a value of $n = 1.420 \pm 0.002$ where the error is the standard deviation extracted from an integrated Gauss fit to the graph (Fig. 8). A virtual focus was seen when beads were immersed in medium with $n=1.43$ and a real focus was observed in suspension with refractive index $n=1.42$. The most precise measurement was obtained by digital holographic microscopy and the measured refractive index $n = 1.423 \pm 0.001$ was used throughout (error is standard error of the mean).

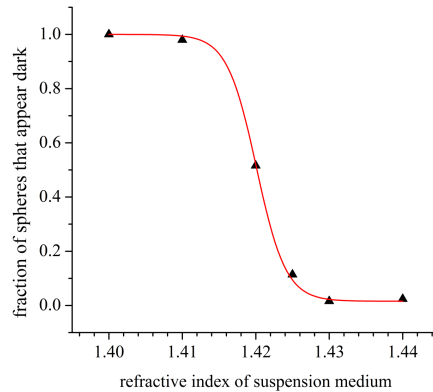


Fig. 8. Determining refractive index of silica microspheres - Method 1. The refractive index can be measured by fitting an integrated Gaussian function (also known as an error function) to a plot of the observed fraction of dark silica beads vs. the refractive index of the suspension medium. The inflection point occurs when the RI of the suspension medium matches the RI of the microspheres. Here, the inflection point of the Boltzmann fit corresponds to $n = 1.4201$ with $R^2 = 0.999$ and $\sigma = 0.002$.

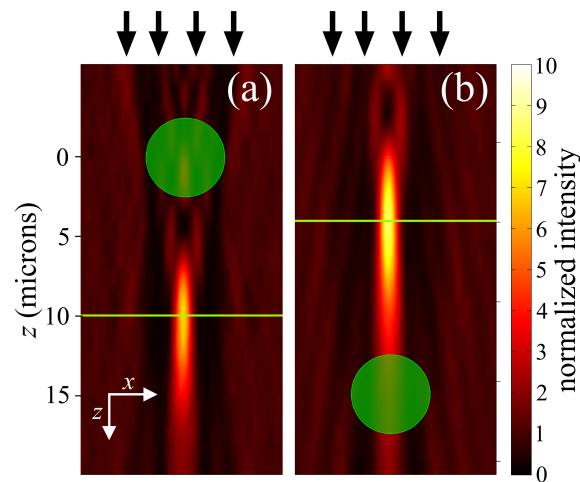


Fig. 9. Determining refractive index of microspheres - Method 2. (a,b) show experimental xz intensity maps for a $5\mu\text{m}$ silica bead suspended in (a) water and (b) oil with refractive index $n = 1.51$. The green horizontal line indicates the focus point and the green circle shows the position and extent of the microsphere. Light incidence position and direction indicated by arrows. The focus point in (b) is an imaginary focus resulting from the diverging lens behaviour of a bead suspended in a medium with a refractive index higher than the bead's. The refractive index of the bead can be determined by suspending the beads in media with different RI and checking whether the focus in the intensity map is below or above the bead.

Acknowledgments

We would like to thank Andreas Reichenbach and Boris Joffe for scientific discussion, Brad Amos for helpful suggestions on the methods of verifying the axial calibration of the employed

microscope, Kevin Chalut for help with the DHM and Kristian Franze for tips on sample preparation. ZB and MK were both funded by the Engineering and Physical Sciences Research Council (UK). MK was additionally funded by the Cambridge European Trust. JG acknowledges financial support through an Alexander von Humboldt Professorship awarded by the Humboldt Foundation.